

1 Growth and form of the mound in Gale Crater, Mars: Slope-  
2 wind enhanced erosion and transport

3 **Authors:** Edwin S. Kite<sup>1\*</sup> and Kevin W. Lewis<sup>2</sup>

4 **Affiliations:**

5 <sup>1</sup>Geological & Planetary Science, California Institute of Technology, MC 150-21, Pasadena CA  
6 91125, USA.

7 <sup>2</sup>Department of Geosciences, Princeton University, Guyot Hall, Princeton NJ 08544, USA.

8 \*Correspondence to: [ekite@caltech.edu](mailto:ekite@caltech.edu)

9

10 **Abstract:** Gale crater, the landing site of the Curiosity Mars rover, hosts a 5 kilometer high  
11 layered mound of uncertain origin which may represent an important archive of the planet's past  
12 climate. Although widely considered to be an erosional remnant of a once crater-filling unit, we  
13 combine structural measurements and a new model of formation to show how this mound may  
14 have grown in place near the center of the crater under the influence of topographic slope-  
15 induced winds. This mechanism implicates airfall-dominated deposition with a limited role for  
16 lacustrine or fluvial activity in the formation of the Gale mound, and is not favorable for the  
17 preservation of organic carbon. Slope-wind enhanced erosion and transport is widely applicable  
18 to a range of similar sedimentary mounds found across the Martian surface.

19

20 **Main text:** In early August 2012 NASA's Mars Science Laboratory (MSL) rover will land in  
21 Gale Crater, Mars. MSL will target a 5km-tall layered sedimentary mound within Gale that is  
22 believed to archive long-term climate change on Mars (*J*). Most of Mars' sedimentary rocks are

23 in the form of intra-crater or canyon mounded deposits like the Gale mound. For example, in the  
24 30km-diameter Endeavour Crater recently entered by the Mars Exploration Rover Opportunity  
25 (2), a thin tongue of sedimentary sulfates is three-quarters encircled by a moat. Intra-crater  
26 mound deposits are not restricted to low latitudes. Radar sounding of crater-filling ice mounds  
27 near the north polar ice sheet shows that they grew from a central core, and are not relicts of a  
28 formerly more extensive ice sheet (3). However, identifying the physical mechanism(s) that  
29 explain the growth and form of equatorial crater mounds has been challenging, in part because  
30 these deposits have no clear analog on Earth. The current prevailing view on the formation of  
31 intra-crater mounds is that sedimentary layers completely filled each crater at least to the summit  
32 of the present-day mound deposit. Subsequent erosion, decoupled from the deposition of the  
33 layers, is invoked to explain the present-day topography. If the sedimentary rocks formed as  
34 subhorizontal layers (4-5), in an evaporitic playa-like setting (6), then  $\gg 10^6 \text{ km}^3$  must have been  
35 removed to produce the modern moats and mounds (7-8). This may cause problems with global  
36 S mass balance (9). This scenario predicts near-horizontal or slightly radially-inward dipping  
37 layers controlled by surface or ground water levels. To test this prediction, we made multiple  
38 measurements of bedding orientation from four separate 1-m scale stereo elevation models from  
39 the High-resolution Imaging Science Experiment (HiRISE) camera, produced by Caltech and the  
40 USGS via the method of Ref. 10. To the contrary, our new structural measurements from  
41 multiple sites around the base of the Gale mound reveal layers with shallow but significant dips  
42 oriented consistently outwards from the mound center (Figure 1; Table S1), suggesting a revised  
43 formation mechanism.

44 Our goal in this paper is to develop the simplest possible model that can account for the  
45 shape and stratigraphy of Mars' sedimentary rock mounds. We assume layers accumulate by the

46 accretion of atmospherically transported sediment, and are destroyed by slope-wind erosion  
47 (Figure 2). Slope-wind enhanced erosion and transport (SWEET) of indurated or lithified  
48 sedimentary materials cannot explain layer orientations at Gale unless the moat seen in Figure 1  
49 was present during mound growth. This implies a coupling between mound primary layer  
50 orientations, slope winds, and mound relief.

51 Mars is a windy place: saltating sand sized particles are in active motion (11), at rates that  
52 predict aeolian erosion of bedrock at 10-50  $\mu\text{m}/\text{yr}$  (12,13). Aeolian erosion of rock has occurred  
53 within the last roughly 1-10 Ka (14) and is probably ongoing. The inability of General  
54 Circulation Models (GCMs) to reproduce these observations shows that small-scale winds, not  
55 the regional-to-global winds resolved by GCMs, are responsible for saltation. Because of Mars'  
56 thin atmosphere, slope winds dominate the circulation in craters and canyons (15,16).  
57 Downslope-oriented yardangs, crater statistics, and hematite lags show that the mounds of Valles  
58 Marineris are being actively eroded by slope winds. Slope-enhanced winds also define both the  
59 large-scale and small-scale topography of the polar layered deposits (17,18). Aeolian processes  
60 were also important on early Mars. Most of the observed sedimentary bedforms at the  
61 Opportunity and Spirit landing sites are sand dune foresets (e.g. 19) and aeolianites likely  
62 represent a volumetrically significant component of the ancient sedimentary rock record,  
63 including within the strata of the Gale mound (20). In places like Becquerel Crater and the upper  
64 portion of the Gale mound, bedding is quasi-periodic and bundled, indicating slow ( $\sim 30 \mu\text{m}/\text{yr}$ )  
65 orbitally-paced accumulation (21). These rates are comparable to the modern gross  
66 atmospherically-transported sediment deposition rate ( $10^{1-2} \mu\text{m}/\text{yr}$ ; e.g. 22) and to the inferred  
67 modern aeolian-abrasion rate, suggesting that aeolian processes may be responsible for the  
68 deposition of the layers. In addition, orbital images of deposits within Valles Marineris show

69 strata that are meters-to-decameters thick, laterally continuous, with horizontal-to-draping layer  
70 orientations, and display very few angular unconformities (e.g., 23). Taken together, slow  
71 accumulation, rarity of unconformities, and draping layer orientations suggest that sedimentary  
72 deposits formed by the accretion of atmospherically-transported sediment (ash, dust, impact  
73 ejecta, ice nuclei, or rapidly-saltating sand) were common on both modern and early Mars (24).

74 In one horizontal dimension ( $x$ ), topographic change  $dz/dt$  is the balance of a net  
75 atmospheric source term  $D$  and erosion  $E$ :

$$76 \quad dz/dt = D(x,t) - E \quad (1)$$

77 Initial model topography in Figure 2 is a basalt (nonerodible) crater/canyon with a flat  
78 floor of half-width  $R$  and long,  $20^\circ$  slopes. To highlight the role of slope winds, we initially  
79 assume  $D$  is constant and uniform (for example, uniform dust concentration multiplied by a  
80 uniform settling velocity, with no remobilization). Sediment induration is probably required to  
81 prevent the atmospheric source term from averaging to zero over long timescales. The necessary  
82 degree of induration is not large: for example, 6-10 mg/g chloride salt increases the threshold  
83 wind stress for saltation by a factor of  $e$  (25). Shallow diagenesis (26) could be driven by  
84 surficial snowmelt or rainfall.

85 We assume that  $E$  depends on the maximum surface shear velocity magnitude,  $U$ :

$$86 \quad E = kU^\alpha \quad (2)$$

87 where  $k$  is an erodibility coefficient and  $\alpha$  is an exponent parameterizing the exponent  
88 relating erosive mass flux to shear velocity. For sand transport, soil erosion, and rock abrasion,  $\alpha$   
89  $\sim 3-4$  (27-29). We assume eroded material does not pile up in the moat but is instead removed  
90 from the crater, for example through breakdown to easily-mobilized dust-sized particles (30).

91 Shear velocity at  $x$  is given by

$$U(x) = U_0 + \max \left| \int_x^{\pm\infty} \frac{\partial z'}{\partial x'} \exp \left( \frac{-|x - x'|}{L} \right) dx' \right|$$

92 (3)

93 where  $U_0$  is synoptic or background shear velocity, and the integral corresponds to a  
 94 contribution from slope winds.  $z'$  is local topography,  $x$  and  $x'$  are distances from the crater  
 95 center,  $L$  is a slope-wind correlation length scale, and the +/- max() operator returns the  
 96 maximum of downslope (nighttime) or upslope (daytime) winds blowing from either the left or  
 97 the right. The slope wind is affected by topography throughout the model domain, but is most  
 98 sensitive to slopes within  $L$  of  $x$ , consistent with analytic and experimental results (31-32)  
 99 showing that the strongest winds occur on steep slopes.  $U_0$  is set to zero in this paper, but large  
 100  $U_0$  does not affect our conclusions. Finally, we define  $D'$  as the deposition rate divided by the  
 101 mean erosion rate on the crater/canyon floor at simulation start.

102 Our model is idealized and excludes both processes that require rover measurements  
 103 (such as grain-size controls, and the source of erosive tools), and processes that will require  
 104 future 3D GCM/mesoscale modeling (such as slope wind dependence on paleoatmospheric  
 105 pressure). Additional numerical diffusivity at the  $10^{-3}$  level is used to stabilize the solution.

106 Results for  $\alpha = 3$ ,  $R/L = 2.4$ ,  $D' = 0.4$  are as follows (Figure 2). Initially (phase I), slope  
 107 winds prevent net accumulation on the crater walls or around the perimeter of the floor. As a  
 108 result, the mound nucleates as a central moat-bounded mesa. Layer orientations in the mesa  
 109 interior are horizontal, steepening near the mesa edge. The mound grows by vertical aggradation  
 110 and can either prograde slightly into the moat or hold position, depending on exact parameter  
 111 values. Aggradation is rapid and aggradation rate does not greatly decrease upsection, consistent  
 112 with observations that do not show a systematic decrease in layer thickness with height (24). The  
 113 dip near the mound flank increases as the mound aggrades vertically. Eventually, slope winds

114 down the growing mound are sufficient to prevent net aggradation at the toe, leading to Phase II  
115 (Figure 2b). During Phase II, mound height continues to increase but mound width decreases due  
116 to flank erosion. Flank erosion is caused by katabatic winds flowing down the growing mound.  
117 Erosion propagates updip, exposing beds deposited during Phase I. When erosion reaches the  
118 mound top, the mound becomes entirely self-destructive (Phase III). Mound height decreases  
119 because flank retreat leads to greater slopes and, therefore, stronger slope winds. Decreasing the  
120 mound height reduces the maximum potential downslope wind. However erosion also decreases  
121 mound width, which helps to maintain steep slopes and correspondingly destructive slope winds.  
122 Topographic change is much slower during Phase III than during Phases I and II.

123         This evolution, which does not require any change in external forcing with time,  
124 describes a clockwise trajectory on a moat width/mound height diagram (Figure 2b). The  
125 systematic exposure of layering on the Gale mound's flanks and upper surface shows that it has  
126 entered Phase III. Flank erosion during later phases tends to remove any unconformities formed  
127 near the edge of the mound, while exposing the stratigraphic record of earlier phases for rover  
128 inspection. Exhumed layers are buried to kilometer depths, but relatively briefly, implying  
129 limited diagenesis of clays and sulfates (*I*). During phase I,  $dz/dt$  is not much slower than  $D$ . If  $D$   
130 corresponds to vertical dust settling at rates similar to today, then we predict that the lower Gale  
131 mound accumulated in  $10^{7-8}$  yr, consistent with dates suggesting that the time represented by the  
132 lower Gale mound is a small fraction of Mars' history (33).

133         Values of  $L$  and  $D'$  on Early Mars are not known, but Gale-like shapes and stratigraphy  
134 arise for a wide range of reasonable parameters (SM Text; Figure S1). Consistent with data  
135 (Figure S2), moats do not extend to basement for small  $R/L$ , and for the largest  $R/L$  multiple  
136 mounds can develop within a single crater.

137  $D$  could vary on timescales that are much shorter than the time for growth of the mound,  
138 for example if Milankovitch cycles set the availability of liquid water for cementation. We set  
139  $D(t) = D(t=0) + D(t=0)\cos(nt)$ , where the oscillation frequency  $n$  is chosen to be faster than the  
140 mound growth timescale. Low-angle unconformities can now be preserved, and the likelihood of  
141 unconformities increases upsection and towards the margin of the moat (Figure 2c). A late-stage  
142 draping layer of sedimentary rock crosscuts layers within the mound core at a high angle, and is  
143 itself broken up by further aeolian erosion. Thin mesa units mapped at Gale and more widely on  
144 Mars have these characteristics (4,20).

145 Deposition at a constant long-term-average rate is unrealistic because the rate of  
146 sedimentary rock formation on Mars is close to zero in the modern epoch, most likely because  
147 atmospheric loss has restricted surface liquid water availability (34-37). Setting  $D'$  to zero after  
148 the crater is incompletely filled allows slope winds down the wall to expose layers and form a  
149 moat, which expands the portion of parameter space that allows moats and mounds to form.

150 Because groundwater-limited evaporite deposition would infill moats and produce near-  
151 horizontal strata, SWEET is incompatible with a global-groundwater water source for early  
152 diagenesis of sedimentary rocks, and with any deposition mechanism that preferentially fills  
153 topographic lows (e.g., fluviodeltaic or lacustrine sedimentation). A top-down water source (ice  
154 weathering, snowmelt, or rainfall) is predicted instead (9,37). Perennial surface liquid water  
155 would shut down saltation and aeolian erosion. Similar to observations along the Opportunity  
156 rover traverse (38), we predict long dry windy periods interspersed by brief wet periods at Gale.  
157 We also predict that the outward-dipping layer orientations in the Gale mound are primary.  
158 Alternative models for the formation of Gale's mound involve landslides, preferential dissolution  
159 of soluble layers near the crater edge, or tectonic tilting, to produce the observed outward dips.

160 When MSL lands in Gale Crater, it can immediately begin to collect observations that will test  
161 our model's predictions, as well as the alternative hypotheses for the mound's formation. For  
162 example, MSL will have the ability to observe evidence for subsurface dissolution within the  
163 crater if it occurred, while measurements of river-deposit tilts and paleoflow directions (e.g.,  
164 from clast imbrication) may constrain post-depositional tilting. MSL can also measure present-  
165 day wind velocity using the Rover Environmental Monitoring System (REMS) instrument, and  
166 image fossilized aeolian bedforms. Unconformities, if present, should be oriented away from the  
167 center of the present mound and should be more frequent upsection. Slow, orbitally-paced  
168 sedimentation and oscillation between reducing and oxidizing conditions would disfavor  
169 preservation of organic carbon.

170

## 171 **References and notes**

172 1. Milliken, R.E., Grotzinger, J.P., Thomson, B.J., 2010, Paleoclimate of Mars as captured by the  
173 stratigraphic record in Gale Crater. *Geophysical Research Letters*, 37, L04201,  
174 doi:10.1029/2009GL041870.

175

176 2. Squyres, S.W., and the Athena Science Team, 2012, Ancient Impact and Aqueous Processes at  
177 Endeavour Crater, Mars. *Science*, 336 (6081), 570-576, doi:10.1126/science.1220476.

178

179 3. Conway, S.J., et al., 2012, Climate-driven deposition of water ice and the formation of  
180 mounds in craters in Mars' North Polar Region. *Icarus*, (in press)

181 doi:10.1016/j.icarus.2012.04.021.



- 182 4. Malin, M.C. and Edgett, K.S., 2000, Sedimentary Rocks of Early Mars. *Science*, 290,1927-  
183 1937, doi:10.1126/science.290.5498.1927.  
184
- 185 5. Montgomery, D.R. and Gillespie, A., 2005, Formation of Martian outflow channels by  
186 catastrophic dewatering of evaporite deposits. *Geology*, 33, 625.  
187
- 188 6. Andrews-Hanna, J.C., Phillips, R.J., Zuber, M.T., 2007, Meridiani Planum and the global  
189 hydrology of Mars. *Nature*, 446, 163-166, doi:10.1038/nature05594.  
190
- 191 7. Zabusky, K. J., Andrews-Hanna, J. C., Wiseman, S. M., 2012, Reconstructing the  
192 Distribution and Depositional History of the Sedimentary Deposits of Arabia Terra, Mars. *Icarus*  
193 (in press), 10.1016/j.icarus.2012.05.007.  
194
- 195 8. Andrews-Hanna, J.C.A., 2012, The formation of Valles Marineris: 3. Trough formation  
196 through super-isostasy, stress, sedimentation, and subsidence. *Journal of Geophysical Research –*  
197 *Planets* (in press), doi:10.1029/2012JE004059.  
198
- 199 9. Michalski, J.R. and Niles, P.B., 2012, An atmospheric origin of Martian Interior Layered  
200 Deposits (ILDs): Links to climate change and the global sulfur cycle. *Geology*, 40, 419-  
201 422, doi:10.1130/G32971.1.  
202

- 203 10. Kirk, R.L., et al., 2008, Ultrahigh resolution topographic mapping of Mars with MRO  
204 HiRISE stereo images: Meter-scale slopes of candidate Phoenix landing sites. *Journal of*  
205 *Geophysical Research*, Volume 113, Issue E12, CiteID E00A24.  
206
- 207 11. Bridges, N.T., et al., 2012a, Planet-wide sand motion on Mars. *Geology*, 40, 31-34,  
208 doi:10.1130/G32373.1.  
209
- 210 12. Bridges, N.T., et al., 2012b, Earth-like sand fluxes on Mars. *Nature*, 485, 339-342,  
211 doi:10.1038/nature11022.  
212
- 213 13. Greeley, R., Iversen, J.D., 1982, *Wind as a geological process on Earth, Mars, Venus, and*  
214 *Titan*, Cambridge University Press.  
215
- 216 14. Golombek, M., et al., 2010, Constraints on ripple migration at Meridiani Planum from  
217 Opportunity and HiRISE observations of fresh craters. *Journal of Geophysical Research*  
218 *(Planets)*, 115, E00F08, doi:10.1029/2010JE003628.  
219
- 220 15. Rafkin, S.C.R., Michaels, T.I., 2003, Meteorological predictions for 2003 Mars Exploration  
221 Rover high-priority landing sites. *Journal of Geophysical Research (Planets)*, 108, 8091,  
222 doi:10.1029/2002JE002027.  
223

- 224 16. Spiga, A. and Forget, F., 2009, A new model to simulate the Martian mesoscale and  
225 microscale atmospheric circulation: Validation and first results. *Journal of Geophysical Research*  
226 (*Planets*), 114(E13), E02009, doi:10.1029/2008JE003242.
- 227
- 228 17. Holt, J.W., et al., 2010, The construction of Chasma Boreale. *Nature*, 465, 446-449.
- 229
- 230 18. Smith, I.B., Holt, J.W., 2010, Onset and migration of spiral troughs on Mars revealed by  
231 orbital radar. *Nature*, 465, 450-453.
- 232
- 233 19. Hayes, A.G., et al., 2011, Reconstruction of eolian bed forms and paleocurrents from cross-  
234 bedded strata at Victoria Crater, Meridiani Planum, Mars. *Journal of Geophysical Research*,  
235 Volume 116, CiteID E00F21.
- 236
- 237 20. Anderson, R.B., Bell, J.F., 2010, Geologic mapping and characterization of Gale Crater and  
238 implications for its potential as a Mars Science Laboratory landing site. *Mars* 5, 76-128,  
239 doi:10.1555/mars.2010.0004.
- 240
- 241 21. Lewis, K.W., et al., 2008, Quasi-Periodic Bedding in the Sedimentary Rock Record of Mars.  
242 *Science*, 322, 1532, doi:10.1126/science.1161870.
- 243
- 244 22. Drube, L., et al., 2010, Magnetic and optical properties of airborne dust and settling rates of  
245 dust at the Phoenix landing site. *Journal of Geophysical Research*, 115, E00E23,  
246 doi:10.1029/2009JE003419.

247

248 23. Fueten, F., et al., 2010, Structural analysis of interior layered deposits in Northern Coprates  
249 Chasma, Mars. *Earth and Planetary Science Letters*, 294, 343-356,  
250 doi:10.1016/j.epsl.2009.11.004.

251

252 24. Cadieux, S.B., Constraining Martian sedimentation via analysis of stratal packaging,  
253 intracrater layered deposits, Arabia Terra, Mars, [http://trace.tennessee.edu/utk\\_gradthes/860](http://trace.tennessee.edu/utk_gradthes/860).

254

255 25. Nickling, W.G., 1984, The stabilizing role of bonding agents on the entrainment of sediment  
256 by wind. *Sedimentology*, 31(1), 111-117. doi: 10.1111/j.1365-3091.1984.tb00726.x.

257

258 26. McLennan, S.M., Grotzinger, J.P., 2008, The sedimentary rock cycle of Mars, *in* Bell, J., III,  
259 editor, *The Martian Surface - Composition, Mineralogy, and Physical Properties: volume 9 of*  
260 *Cambridge Planetary Science Series*, Cambridge University Press, 2008, p. 541.

261

262 27. Lu , H., and Shao, Y., 1999, A new model for dust emission by saltation bombardment.  
263 *Journal of Geophysical Research*, 104, 16,827-16,842.

264

265 28. Wang, Z.-T., Wang, H.-T., Niu, Q.-H., Dong, Z.-B. and Wang, T., 2011, Abrasion of  
266 yardangs. *Physical Review E*, 84, 031304.

267

268 29. Kok, J.F., Parteli, E.J.R., Michaels, T.I., and Karam, D. B., 2012, The physics of wind-blown  
269 sand and dust. *Reports on Progress in Physics*, preprint available at:

270 [http://sitemaker.umich.edu/jasperkok/files/kok\\_etal\\_2012\\_physics\\_of\\_windblown\\_sand\\_and\\_du](http://sitemaker.umich.edu/jasperkok/files/kok_etal_2012_physics_of_windblown_sand_and_dust.pdf)  
271 [st.pdf](http://sitemaker.umich.edu/jasperkok/files/kok_etal_2012_physics_of_windblown_sand_and_dust.pdf).

272

273 30. Sullivan, R., et al., Wind-driven particle mobility on Mars: Insights from Mars Exploration  
274 Rover observations at "El Dorado" and surroundings at Gusev Crater. *Journal of Geophysical*  
275 *Research*, 113(E6), E06S07.

276

277 31. Manins, P. C., Sawford, B. L., 1987, A model of katabatic winds. *Journal of Atmospheric*  
278 *Sciences*, 36, 4, pp.619-630.

279

280 32. Parish, T.R., Bromwich, D.H., 1987, The surface windfield over the Antarctic ice sheets.  
281 *Nature* 328, 51-54, doi: 10.1038/328051a0.

282

283 33. Zimbelman, J.R., Scheidt, S.P., 2012, Hesperian Age for Western Medusae Fossae  
284 Formation, Mars. *Science*, doi: 10.1126/science.1221094.

285

286 34. Knoll, A.H., et al., 2008, Veneers, rinds, and fracture fills: Relatively late alteration of  
287 sedimentary rocks at Meridiani Planum, Mars. *Journal of Geophysical Research*, Volume 113,  
288 Issue E6, CiteID E06S16.

289

290 35. Tosca, N.J., Knoll, A.H., 2009. Juvenile chemical sediments and the long term persistence of  
291 water at the surface of Mars. *Earth and Planetary Science Letters* 286(3-4): 379-386.

292 doi:10.1016/j.epsl.2009.07.004

293

294 36. Andrews-Hanna, J.C., Lewis, K.W., 2011, Early Mars Hydrology: 2. Hydrological evolution  
295 in the Noachian and Hesperian epochs. *J. Geophys. Res.*, 116, E02007,  
296 doi:10.1029/2010JE003709.

297

298 37. Kite, E.S., Halevy, I., Kahre, M.A., Wolff, M.J., Manga, M., 2012, Seasonal melting and the  
299 formation of sedimentary rocks on Mars, with predictions for the Gale Crater mound. Submitted  
300 to *Icarus*, <http://arxiv.org/abs/1205.6226>.

301

302 38. Metz, J.M., et al., 2009, Sulfate-Rich Eolian and Wet Interdune Deposits, Erebus Crater,  
303 Meridiani Planum, Mars. *Journal of Sedimentary Research*, 79, 247-264,  
304 doi:10.2110/jsr.2009.033.

305

306 39. Thomson, B.J., et al., 2011, Constraints on the origin and evolution of the layered mound in  
307 Gale Crater, Mars using Mars Reconnaissance Orbiter data. *Icarus*, 214, 413 – 432.

308

309 40. Trachte, K., Nauss, T., Bendix, J., 2010, The impact of different terrain configurations on the  
310 formation and dynamics of katabatic flows: idealized case studies. *Boundary-Layer  
311 Meteorology*, 134, 307-325.

312

313 41. Ye, Z.J., Segal, M., Pielke, R.A., 1990, A comparative study of daytime thermally induced  
314 upslope flow on Mars and Earth. *Journal of the Atmospheric Sciences*, 47, 612-628.

315

316 42. Savijarvi, H., Siili, T., 1993, The Martian slope winds and the nocturnal PBL jet. Journal of  
317 the Atmospheric Sciences, 50, 77-88.

318

319 43. Siili, T., Haberle, R.M., Murphy, J.R., Savijarvi, H., 1999, Modelling of the combined late-  
320 winter ice cap edge and slope winds in Mars' Hellas and Argyre regions. Planetary and Space  
321 Science, 47, 951-970.

322

323 44. Ellison, T.H., Turner, J.S., 1959, Turbidity entrainment in stratified flows. J. Fluid Mech. 6,  
324 423-48.

325

326 45. Manins, P. C., Sawford, B. L., 1979, A Model of Katabatic Winds. Journal of Atmospheric  
327 Sciences, 36, 619-630.

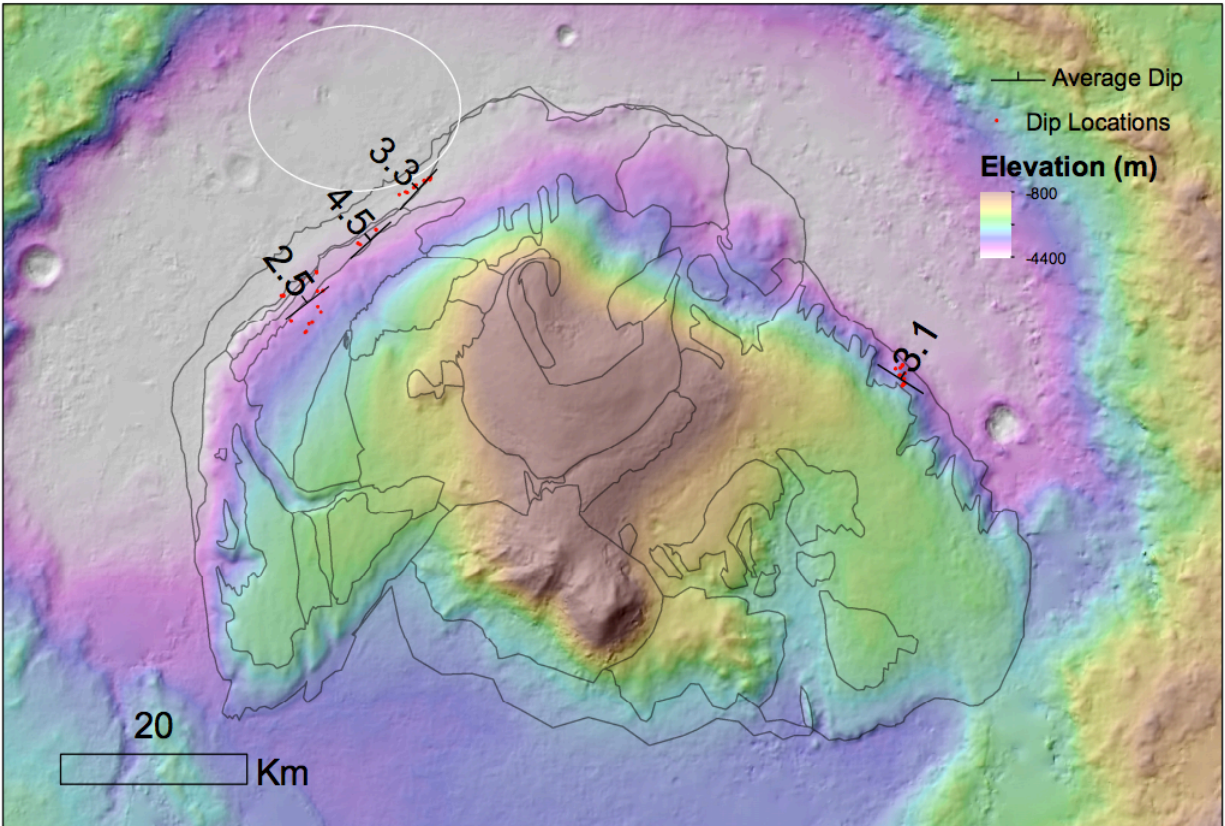
328

329 46. Horst, T. W., Doran, J. C., 1986, Nocturnal drainage flow on simple slopes. Boundary-Layer  
330 Meteorology, 34, 263-286

331

332

333 **Acknowledgements:** We thank Mike Lamb, Claire Newman, Mark Richardson, Bill Dietrich,  
334 Woody Fischer, and especially Kathryn Stack, for their intellectual contributions.



335

336

**Fig. 1.** Bedding orientation measurements from four locations around the margin of the Gale

337

crater mound. Individual measurements are marked in red, with the average at each site

338

indicated by the dip symbol. At each location, beds consistently dip away from the center of the

339

mound, consistent with the proposed model. Background elevation data is from the High-

340

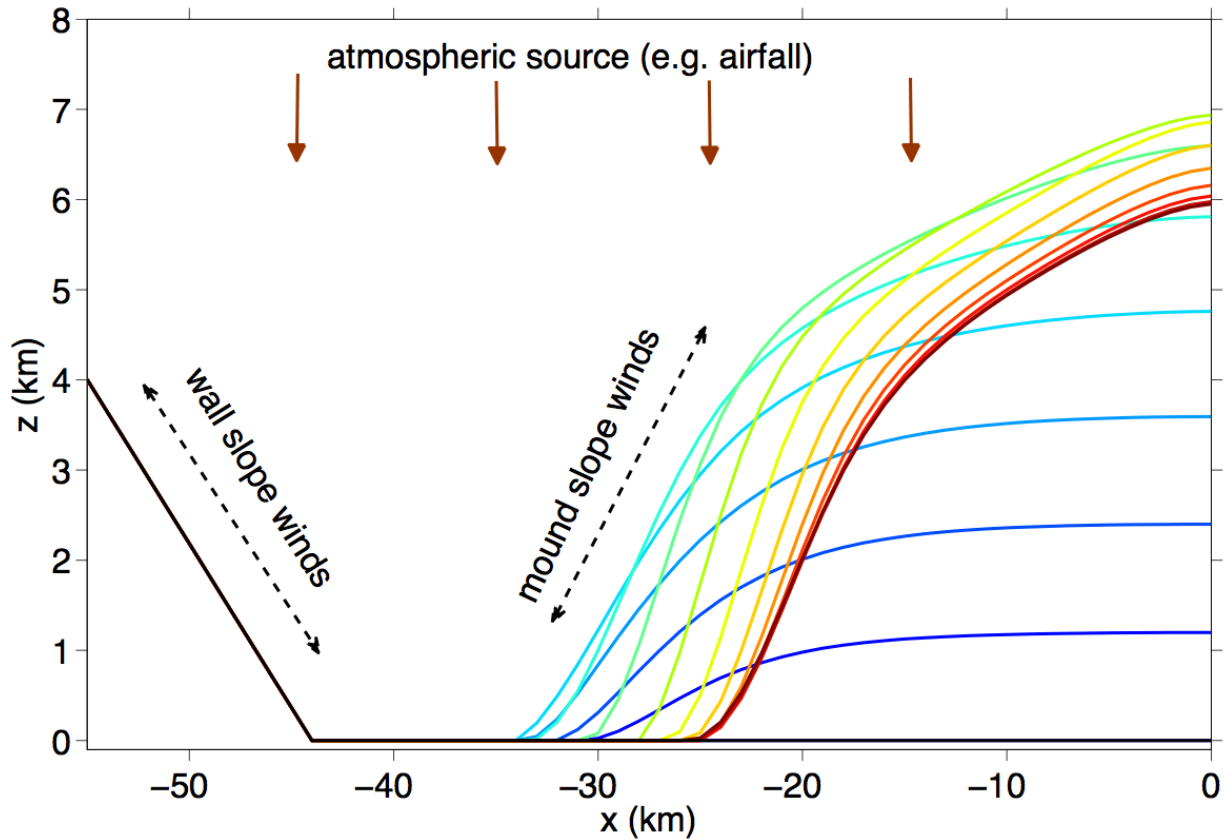
Resolution Stereo Camera (HRSC) (<http://europlanet.dlr.de/node/index.php?id=380>), with

341

superimposed geologic units from Ref. 39. The MSL landing ellipse is shown in white.

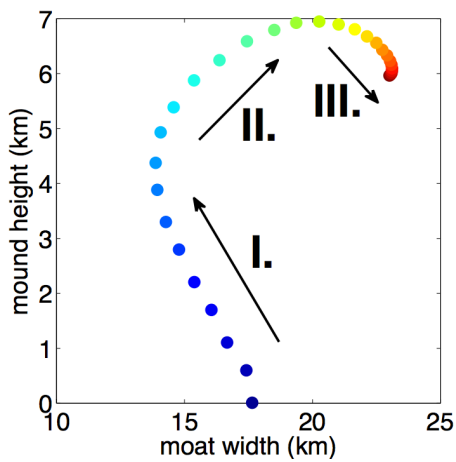


342 (A)



343

344 (B)

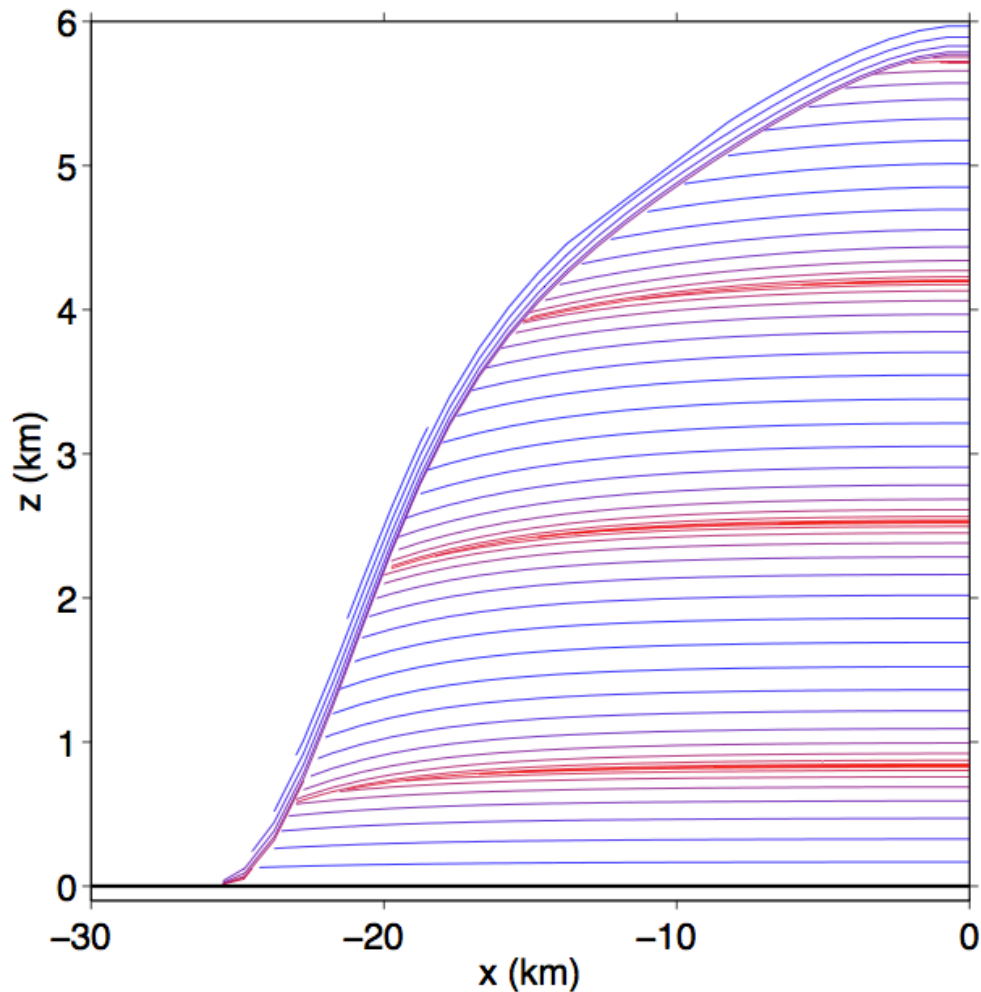


345

346 **Fig. 2.** Simulated sedimentary mound growth and form. Colored lines in (A) correspond to  
347 snapshots of the mound surface equally spaced in time (blue being early and red being late). The  
348 black line corresponds to the initial topography. (B) shows mound geometry, with two colored

349 dots for every colored line in (A). I, II, and III correspond to phases in the evolution of the  
350 mound. (A) and (B) are for steady uniform deposition. Results for time-varying uniform  
351 deposition appear very similar at this scale.

352 (C)



353  
354 (C) shows stratigraphy resulting from sinusoidally time-varying deposition. For clarity, only a  
355 small number of oscillations are shown. Color of strata corresponds to deposition rate: blue is  
356 high  $D$ , which might correspond to wet climates (36,37), and red is low  $D$ , which might  
357 correspond to dry climates (36,37). Note low-angle unconformities, and late-stage flanking unit  
358 intersecting the mound core at a high angle.

359 **Supplementary materials**

360 Controls on mound growth and form

361  $L$  will vary across Mars because of changing 3D topography (40), and will vary in time because  
362 of changing atmospheric density. Ref. 41 shows  $L \sim 20\text{km}$  for Mars slopes with negligible  
363 geostrophic effects. Simulations of gentle Mars slope winds strongly affected by the Coriolis  
364 force suggest  $L \sim 50\text{-}100\text{ km}$  (42-43). Entrainment acts as a drag coefficient with value 0.02-0.05  
365 for Gale-relevant slopes (44-46), suggesting  $L = 20\text{-}50\text{ km}$  for a 1km thick cold boundary layer.  
366 Therefore  $L \sim 10^{1-2}\text{ km}$  is reasonable, but there is considerable uncertainty, which we explore in  
367 the next section using a parameter sweep.

368 To determine the effect of parameter choices on sedimentary rock mound shape, size,  
369 stratigraphy and exposure, we carried out a parameter sweep in  $\alpha$ ,  $D'$ , and  $R/L$  (Figure S1). Weak  
370 slope dependence ( $\alpha = 0.05$ ) is sufficient to produce strata that dip toward the foot of the  
371 crater/canyon slope (like a sombrero hat). Similarly weak *negative* slope dependence ( $\alpha = -0.05$ )  
372 is sufficient to produce concave-up fill.

373 At low  $R/L$  (i.e., small craters) or at low  $\alpha$ ,  $D'$  controls overall mound shape and slope  
374 winds are unimportant. When  $D'$  is high, layers fill the crater; when  $D'$  is low, layers do not  
375 accumulate. When either  $\alpha$  or  $R/L$  or both are  $\gg O(1)$ , slope wind enhanced erosion and  
376 transport dominates the behavior. Thin layered crater floor deposits form at low  $D'$ , and large  
377 mounds at high  $D'$ . At high  $R/L$  and high  $\alpha$  (large craters and knickpointlike erosion), multiple  
378 mounds form at late time.

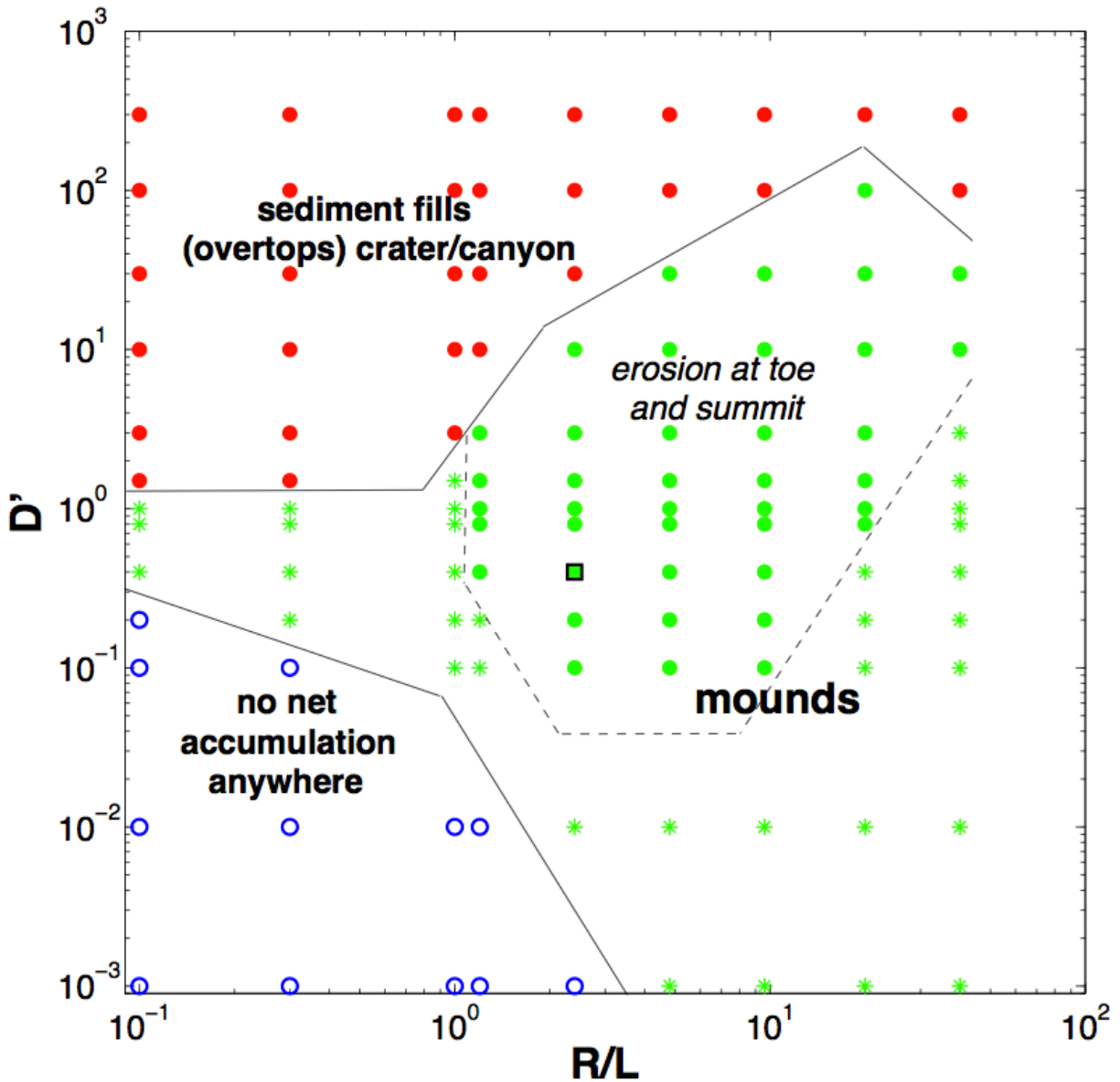
379 If  $L$  is approximated as being constant across the planet, then  $R/L$  is proportional to  
380 crater/canyon size. Moats do not extend to basement for small  $R/L$ , although there can be a small  
381 trench at the break-in slope. For larger  $R/L$ , moats form, and for the largest craters/canyons,

382 multiple mounds can develop within a single crater because slope winds break up the deposits.  
383 This is consistent with data which suggest a universal length scale for mound size (Figure S2).  
384 Small exhumed craters in Meridiani show concentric layering consistent with concave-up dips.  
385 Larger craters across Meridiani Planum, together with Gale and Nicholson Craters, the smaller  
386 Valles Marineris chasmata, and the north polar ice mounds, show a single mound. The largest  
387 canyon system on Mars (Ophir-Candor-Melas) shows multiple mounds per canyon. Steeper wall  
388 slopes in the model tend to push mound break-up to larger sizes. Gale-like mounds (with erosion  
389 both at the toe and the summit) are most likely for high  $R/L$ , high  $\alpha$ , and intermediate  $D'$  (high  
390 enough for some accumulation, but not so high as to fill the crater) (Figure S1). These sensitivity  
391 tests suggest that mounds with erosion both at the toe and the summit are a generic outcome of  
392 steady uniform deposition modified by slope-wind enhanced erosion and transport for estimated  
393 Early Mars parameter values.

394

#### 395 Sequence stratigraphy on Mars

396 Sequence stratigraphy on Earth divides sedimentary deposits into genetically related packages  
397 bounded by hiatuses controlled by sediment supply, subsidence, and changes in base level. On  
398 the basis of our model results (Figure 2c), we suggest a Martian equivalent for the deposition of  
399 layered deposits in which the primary control is not base-level change, but changes in the ability  
400 of the climate system to indurate and cement atmospherically-transported sediment (e.g., 36-37).  
401 Rare wet periods provide an opportunity for mound accumulation, and these sequences are  
402 bounded by surfaces of nondeposition that represent mound degradation during more common  
403 dry periods. These oscillations may be orbitally paced, although the time represented by each  
404 sequence is unknown.



405

406 **Figure S1.** Overall growth and form of sedimentary mounds – results from a model parameter

407 sweep varying  $R/L$  and  $d'$ , with fixed  $\alpha = 3$ . Black square corresponds to the results shown in

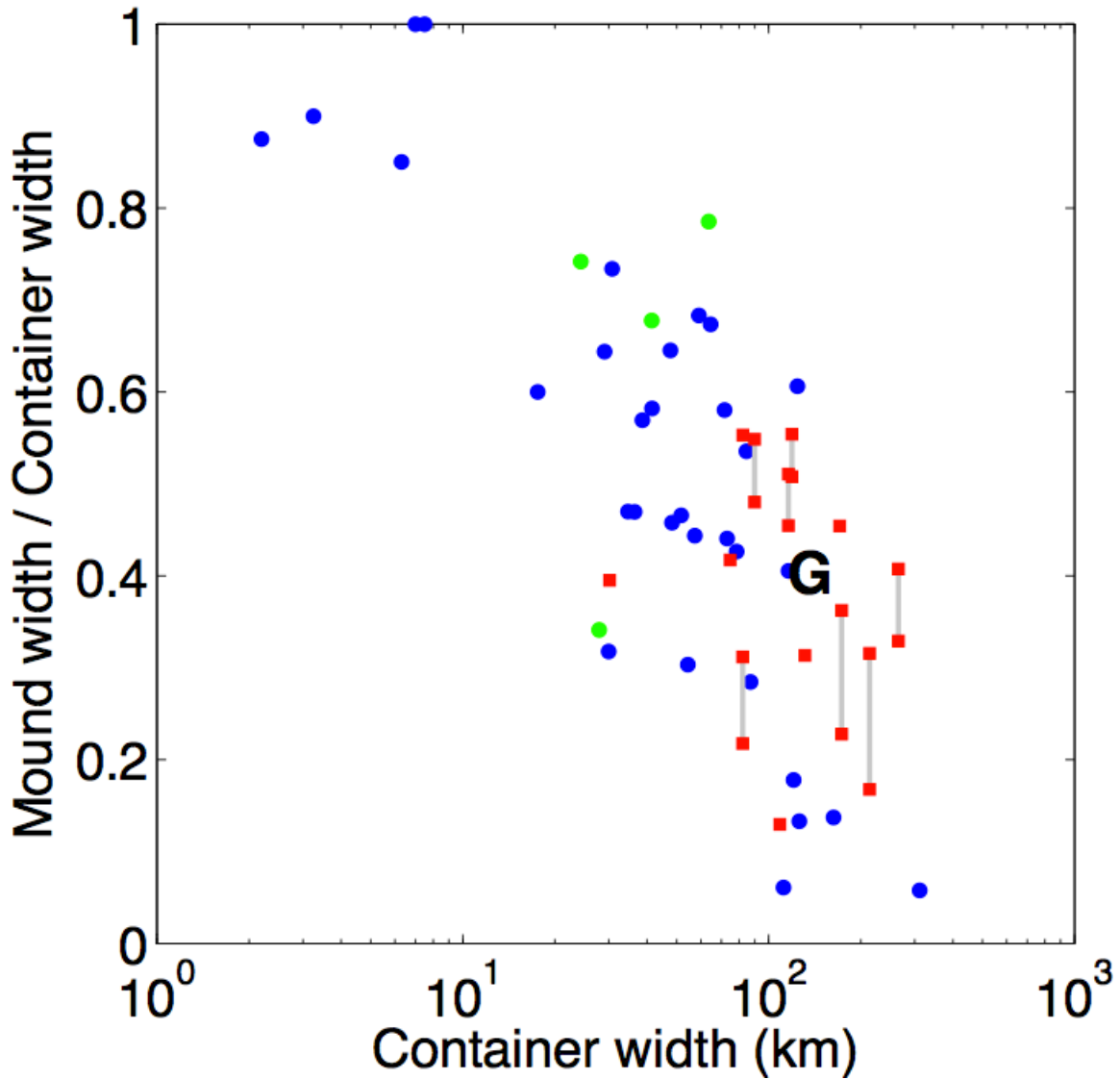
408 more detail in Figure 2. Symbols correspond to the overall results:– no net accumulation of

409 sediment anywhere (blue open circles); sediment overtops crater/canyon (red filled circles);

410 mound forms and remains within crater (green symbols). Green filled circles correspond to

411 outcomes where layers are exposed at both the toe and the summit of mound, similar to Gale.

412 Multiple mounds form in some of these cases (see Supplementary Text).



413  
 414 **Figure S2.** Width of largest mound does not keep pace with increasing crater/canyon width,  
 415 suggesting a length threshold beyond which slope winds break up mounds. Blue dots correspond  
 416 to nonpolar crater data, red squares correspond to canyon data, and green dots correspond to  
 417 polar ice mound data. Gray vertical lines show range of uncertainty in largest-mound width for  
 418 Valles Marineris canyons. “G” corresponds to Gale Crater. Craters smaller than 10km were  
 419 measured using CTX or HiRISE. All other craters, canyons and mounds were measured using  
 420 the THEMIS global day IR mosaic on a MOLA base. Width is defined as polygon area divided  
 421 by the longest straight-line length that can be contained within that polygon.

422 **Table S1.** Layer orientation measurements summarized in Figure 1.

Lon (°)	Lat (°)	Z (m)	Dip (°)	Dip Az. (°)	HiRISE Image ID
138.3949	-5.0223469	-3263.1	3.53	30.68	PSP_008437_1750
138.39266	-5.0238771	-3201.9	2.52	62.01	PSP_008437_1750
138.38631	-5.0158761	-3216.9	2.10	94.68	PSP_008437_1750
138.38702	-5.0155078	-3201.4	7.31	41.72	PSP_008437_1750
138.39168	-4.9983579	-3554.2	2.06	54.81	PSP_008437_1750
138.3878	-5.0030348	-3429.9	0.43	-21.29	PSP_008437_1750
138.37991	-5.0045169	-3425.8	5.04	89.54	PSP_008437_1750
138.37958	-5.0041789	-3434.5	3.79	70.24	PSP_008437_1750
138.39253	-4.9974918	-3583.8	4.65	51.98	PSP_008437_1750
138.39671	-5.0123743	-3421.5	4.14	47.28	PSP_008437_1750
138.39559	-5.0314236	-3290.1	4.07	40.92	PSP_008437_1750
138.39618	-5.0301064	-3308.2	2.55	76.18	PSP_008437_1750
138.39374	-5.03171	-3260.1	3.24	43.31	PSP_008437_1750
138.39205	-5.0351893	-3176.3	2.07	75.25	PSP_008437_1750
138.3917	-5.0350616	-3173.3	2.21	86.77	PSP_008437_1750
137.49485	-4.6858121	-4098.5	3.34	148.1	ESP_023957_1755
137.49197	-4.6847781	-4103.8	3.98	174.47	ESP_023957_1755
137.48052	-4.6893313	-4101.3	6.06	132.82	ESP_023957_1755
137.53315	-4.6593871	-4120.3	6.48	114.03	ESP_023957_1755
137.5374	-4.6588595	-4108.2	0.50	13.56	ESP_023957_1755

137.53552	-4.6621189	-4073.1	3.90	-149.05	ESP_023957_1755
137.52567	-4.6641024	-4127.1	7.16	130.19	ESP_023957_1755
137.52487	-4.6636562	-4138.3	4.83	152.05	ESP_023957_1755
137.52653	-4.6655284	-4101.1	4.59	-153.08	ESP_023957_1755
137.50615	-4.676802	-4083.2	2.32	83.97	ESP_023957_1755
137.51028	-4.6721369	-4128.0	3.24	91.62	ESP_023957_1755
137.27098	-4.8715007	-3849.6	1.09	10.19	PSP_001488_1750
137.26671	-4.871837	-3857.7	5.19	85.97	PSP_001488_1750
137.27073	-4.8726906	-3833.2	2.61	-51.44	PSP_001488_1750
137.28434	-4.9179523	-3513.9	6.78	136.55	PSP_001488_1750
137.33063	-4.8310273	-3768.9	2.16	140.09	PSP_001488_1750
137.33036	-4.8285655	-3792.5	2.65	143.84	PSP_001488_1750
137.30338	-4.8466422	-3802.8	4.38	124.94	PSP_001488_1750
137.30307	-4.8457244	-3815.7	4.51	111.27	PSP_001488_1750
137.30442	-4.8455009	-3799.2	2.34	79.11	PSP_001488_1750
137.33242	-4.8638848	-3507.1	2.04	132.56	PSP_001488_1750
137.31164	-4.9369596	-3278.4	3.74	129.01	PSP_001488_1750
137.30984	-4.9389356	-3287.6	4.46	119.79	PSP_001488_1750
137.32216	-4.9201255	-3290.9	1.79	134.69	PSP_001488_1750
137.31702	-4.922859	-3306.6	4.20	160.7	PSP_001488_1750
137.33822	-4.901912	-3265.6	4.87	-174.83	PSP_001488_1750
137.3328	-4.8924006	-3389.9	6.71	117.93	PSP_001488_1750
137.3421	-4.8631512	-3464.4	5.66	105.35	PSP_001488_1750



137.40969	-4.7799276	-3656.9	3.69	167.09	PSP_009149_1750
137.40533	-4.7770286	-3736.8	2.13	168.14	PSP_009149_1750
137.43867	-4.7530302	-3810.1	6.07	128.67	PSP_009149_1750
137.4381	-4.7521312	-3823.7	5.92	123.62	PSP_009149_1750

423